

1           **Simulations of gravitoelastic correlations for the**  
2           **Sardinian candidate site of the Einstein Telescope**

3                           **Tomislav Andric<sup>1,2</sup> and Jan Harms<sup>1,2</sup>**

4                                   <sup>1</sup>Gran Sasso Science Institute (GSSI), I-67100 L'Aquila, Italy  
5                                   <sup>2</sup>INFN, Laboratori Nazionali del Gran Sasso, I-67100 Assergi, Italy

6           **Key Points:**

- 7           • Spectral-element simulation can be used to calculate gravitoelastic correlations  
8           of ambient seismic fields  
9           • Topography at Sardinian candidate site of Einstein Telescope has significant im-  
10          pact on gravitoelastic correlations  
11          • Topography at Sardinian site acts as low-pass filter for Rayleigh waves

---

Corresponding author: Tomislav Andric, [tomislav.andric@gssi.it](mailto:tomislav.andric@gssi.it)

**Abstract**

Gravity fluctuations produced by ambient seismic fields are predicted to limit the sensitivity of the next-generation, gravitational-wave detector Einstein Telescope at frequencies below 20 Hz. The detector will be hosted in an underground infrastructure to reduce seismic disturbances and associated gravity fluctuations. Additional mitigation might be required by monitoring the seismic field and using the data to estimate the associated gravity fluctuations and to subtract the estimate from the detector data, a technique called coherent noise cancellation. In this paper, we present a calculation of correlations between surface displacement of a seismic field and the associated gravitational fluctuations using the spectral-element SPECFEM3D Cartesian software. The model takes into account the local topography at a candidate site of the Einstein Telescope at Sardinia. This paper is a first demonstration of SPECFEM3D's capabilities to provide estimates of gravitoelastic correlations, which are required for an optimized deployment of seismometers for gravity-noise cancellation.

**1 Introduction**

The third-generation gravitational-wave (GW) observatory, Einstein Telescope (ET) (ET Science Team, 2011), will have about an order of magnitude better sensitivity over almost the entire GW observation band compared to current generation detectors Virgo (Acernese et al., 2015), LIGO (Abbott et al., 2016), KAGRA (Akutsu et al., 2019), and LIGO India (Souradeep, 2016). Newtonian noise (NN) constitutes one of the fundamental infrastructure limitations, which affects the sensitivity of GW detectors. NN originates from fluctuations in the surrounding geological and atmospheric densities, causing a variation in the gravitational field and these gravity fluctuations act on the test masses (TM) causing detector noise mostly below 30 Hz (Harms, 2019). A large sensitivity improvement is targeted with ET in the infrasound observation band (1 to 20 Hz), where current generations of detectors have no detection capabilities. This will increase the number and signal-to-noise ratio of observable GW signals and therefore significantly enhance the astrophysical impact of third-generation observatories (Hild et al., 2011; Maggiore et al., 2020). In the frequency band below 30 Hz, it is possible to follow better the inspiral phase of compact binaries composed of neutron stars (NS) and stellar-mass black holes (BH), or open the window to observations of intermediate-mass black holes (IMBH). It is possible to follow the waveform evolution for a longer amount of time and this practically means: more accurate estimates of some of the binary system's parameters including its sky location (Grimm & Harms, 2020), and potentially an early warning for the electromagnetic (EM) follow-up of these sources (Chan et al., 2018). Einstein Telescope will also be sensitive to continuous GW emission from a large population of spinning NSs below 10 Hz (Sathyaprakash et al., 2012). Therefore, there is a strong scientific drive to expand the detection band and to improve the sensitivity down to lower frequencies.

The dominant noise sources at very low frequencies are those associated with the seismic motion that couples with the detector. One mechanism is the mechanical transmission, where ground vibrations perturb the motion of the TM via the TM suspension system. This is known as seismic noise. Elaborated vibration-isolation systems are used to suspend the TM, significantly reducing seismic disturbances within the detection band (Acernese et al., 2010; Matichard et al., 2014). Another mechanism is by gravitational coupling giving rise to NN and cannot be shielded in any way (M. Beker et al., 2011; M. G. Beker et al., 2015). A well-explored cancellation scheme is based on Wiener filters (Cella, 2000; Badaracco & Harms, 2019). Wiener filters are linear filters calculated from the correlation between the reference and target channels (Orfanidis, 2007). In the context of seismic NN cancellation, the sensors (seismometers) monitor seismic fields, which means that correlations between them are to be expected (Harms, 2019).

63 Most of the seismic noise is generated near the surface and it generally decreases  
 64 significantly with depth. Predictions based on a detailed characterization of the LIGO  
 65 sites show that seismic surface fields give the dominant contribution to NN (Driggers et  
 66 al., 2012). Accordingly, a NN cancellation scheme can be realized using an array of seis-  
 67 mometers deployed at the surface near the TM (Coughlin et al., 2016). The construc-  
 68 tion of ET has been proposed to be underground, where the amount of seismic motion  
 69 is expected to be lower and more stable (Harms et al., 2010; M. G. Beker et al., 2015;  
 70 Mandic et al., 2018). NN is about two orders of magnitude less underground which is  
 71 substantial (Amann et al., 2020).

72 One of the most important things in NN cancellation is the homogeneity of the seis-  
 73 mic field. Scattering of seismic fields from an irregular surface topography can cause het-  
 74 erogeneity of the seismic field. It can lead to a more complex field structure that is not  
 75 completely characterized by surface displacement and will likely pose a great challenge  
 76 even to 3D seismic surveys with boreholes where effective placement of seismometers needs  
 77 to be achieved (Badaracco & Harms, 2019). The scattering will especially be the prob-  
 78 lem if it is strong enough to alter seismic waveforms significantly over very short propa-  
 79 gation distances (Driggers et al., 2012). Even if it is identified and fully characterized,  
 80 scattering could pose a serious challenge to NN subtraction, since it might increase the  
 81 required effort and therefore cost of a NN mitigation system. Issues of topographic scat-  
 82 tering and its connection to NN cancellation are partly examined in (Coughlin & Harms,  
 83 2012). They found that the total contribution of waves scattered from topography can  
 84 be high, which makes topographic scattering relevant to NN subtraction in future low-  
 85 frequency GW detectors. Seismic scattering was investigated analytically in numerous  
 86 publications, see for example (Gilbert & Knopoff, 1960; Abubakar, 1962, 1963; J. A. Hud-  
 87 son, 1967; Ogilvy, 1987). An extensive and conclusive study of the impact of topogra-  
 88 phy scattering on coherent cancellation has not been carried out so far.

89 In this paper, we simulate synthetic ambient-noise cross-correlations between sta-  
 90 tions at the surface of a finite-element model using a 3D spectral-element method (SEM)  
 91 implemented in SPECFEM3D Cartesian software (Komatitsch & Tromp, 2002a, 2002b;  
 92 Komatitsch et al., 2018). Cross-correlations are simulated for the flat model and for the  
 93 topographic model using elevation data at the three (foreseen) vertices of the proposed  
 94 ET site at Sardinia. Using these correlations we show the effects of topographic scatter-  
 95 ing on seismic coherence and on correlations between test mass acceleration and verti-  
 96 cal seismic surface displacement. These correlations are crucial in Wiener-filter construc-  
 97 tion. One of the main goals in the future will be to investigate whether high noise can-  
 98 cellation through Wiener filtering or similar methods will be effective at the Sardinia site  
 99 for ET.

100 In section 2, the ET detector and the ET candidate site at Sardinia are briefly pre-  
 101 sented. In section 3, our main analysis tools SPECFEM3D Cartesian and Trellis are in-  
 102 troduced. In section 4, the building of the finite-element model is described. In section  
 103 5, the theory of noise cross-correlation is reviewed with focus on the method implemented  
 104 in SPECFEM3D. In section 6, ensemble sensitivity kernels and their importance are ex-  
 105 plained. In section 7, we present the main results of our study concerning the effect of  
 106 topographic scattering on seismic correlations and the prediction of gravitational cou-  
 107 pling between seismic surface displacement and an underground test mass.

## 108 **2 Einstein Telescope and Sardinia site**

109 The third-generation GW observatory, ET, will be aiming to reach a sensitivity for  
 110 GW signals emitted by astrophysical and cosmological sources about a factor of 10 bet-  
 111 ter than current detectors over much of the observation band (ET Science Team, 2011).  
 112 As all of the GW detectors so far, ET will be a modified Michelson interferometer with  
 113 suspended mirrors that act as TMs. These instruments behave as transducers to con-

114 vert the space-time strain caused by a GW to fluctuations in optical power (Barsotti et  
 115 al., 2019). In its final construction stage, ET should consist of three nested detectors,  
 116 built a few 100 m underground, which would be arranged in a triangular pattern. Ad-  
 117 vantages of ET with respect to the traditional L-shaped geometry of current GW detec-  
 118 tors are that it will have a more uniform antenna pattern and be sensitive to both GW  
 119 polarizations independent of the wave-propagation direction. The overall frequency range  
 120 will reach from a few Hertz to about 10 kHz. Each individual detector will comprise two  
 121 interferometers forming a so-called xylophone configuration (Hild et al., 2009), one spe-  
 122 cialized for detecting low-frequency GWs (low laser power, low temperature; frequency  
 123 range from 3 Hz to 50 Hz) and the other one for the high-frequency part (room temper-  
 124 ature, high laser power, frequency range from 50 Hz to 10 kHz).

125 For the reduction of NN, a detector site with weak gravity fluctuations should be  
 126 chosen. High-frequency seismic spectra (above a few Hertz) are all significantly quieter  
 127 underground than at typical surface sites. This can be explained by the exponential fall  
 128 of Rayleigh-wave amplitudes combined with the fact that high-frequency seismicity is  
 129 typically generated at the surface, and most surface sites are covered by a low-velocity  
 130 layer of unconsolidated ground. Also, underground sites are attractive since the risk that  
 131 seismicity will change in the future is lower, while surface sites can in principle change  
 132 seismicity over the course of many years, because of anthropogenic factors. Addition-  
 133 ally, atmospheric gravity perturbations are strongly suppressed underground (Fiorucci  
 134 et al., 2018).

135 The selected site should offer the possibility for efficient coherent cancellation of  
 136 NN with surface and borehole seismometer deployment. Two-point spatial correlation  
 137 of the seismic field determines the efficiency of a cancellation scheme. The strongest scat-  
 138 terer of seismic waves above a few Hz is the surface with rough topography (strong to-  
 139 pographic gradients). If scattering is significant then correlation can be strongly altered,  
 140 and a seismic array consisting of a potentially large number of seismometers needs to be  
 141 deployed with difficult to determine sensor positions (Harms, 2019). Since the ground  
 142 medium close to the TM at the Sardinia site is fairly uniform, high scattering cross sec-  
 143 tions are unlikely to be observed for underground propagation of seismic waves (Driggers  
 144 et al., 2012). Still, heterogeneity of the ground may add complexity, and a refined model  
 145 should include information about local geology.

146 The suggested site at Sardinia (Italy) is near the city Lula (figure 1) with vertex  
 147 coordinates given in table 1. Spectral density of the Sardinia site ambient seismic field  
 148 is close to Peterson’s New Low Noise Model (NLNM) (M. G. Beker et al., 2012). Also,  
 149 what goes in favor of the Sardinia site is the fact that the most seismically quiet sites  
 150 are found in hard rock geologies and the Sardinia site is mostly made of granite and schist.  
 151 In terms of the construction of underground facilities, rock stability is a crucial factor,  
 152 which then tends to be more favorable in hard rock (M. G. Beker et al., 2015). This is  
 153 disadvantageous for NN reduction with depth, which decreases exponentially with in-  
 154 creasing seismic-wave speed. Coordinates of vertices were chosen taking into consider-  
 155 ation the quality of the rocks.

156 These vertices make an equilateral triangle with approximately 10.7 km side length.  
 157 Surface areas of  $3 \text{ km} \times 3 \text{ km}$  size with topographies where the respective ET vertex is  
 158 located under the center point of the area are given in figure 2. The resolution of ele-  
 159 vation data is 30 m. For examination of seismic coherence and gravity-displacement cor-  
 160 relations, due to high computational costs, we chose only vertex A3 because it has the  
 161 roughest surrounding topography (figure 2c) among all three vertices and therefore the  
 162 largest scattering potential. Roughness can for example be quantified by the rms of the  
 163 elevation data, which are 52.4 m, 43.5 m, 129.6 m for the vertices A1, A2, A3, respectively.  
 164 As already said, scattering causes heterogeneity of the seismic field, which will be one  
 165 of the main problems in NN cancellation. If the problem of NN description and cancel-

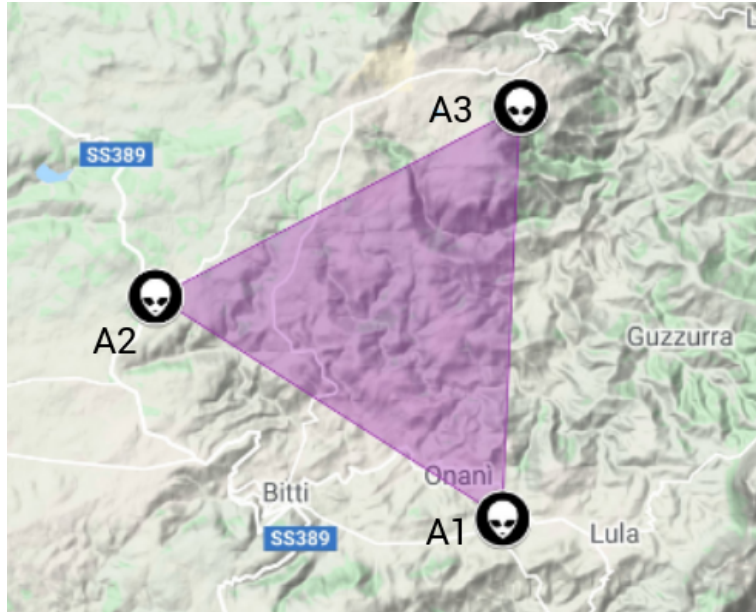


Figure 1: Sardinia candidate site for Einstein Telescope with marked vertex locations.

Cavern	Latitude	Longitude
A	40°28'21.11"	9°27'18.78"
B	40°31'27.73"	9°20'54.84"
C	40°34'08.24"	9°27'38.82"

Table 1: Coordinates of vertices of Einstein Telescope.

166 lation is understood for vertex A3, there will not be any additional challenges when re-  
 167 peating the analysis for vertices A1 and A2.

### 168 3 Finite-element simulation and model meshing

169 SPECFEM3D Cartesian is a powerful software package for seismic-wave propaga-  
 170 tion modeling at local and regional scales based upon the spectral-element method (SEM)  
 171 (Komatitsch & Tromp, 1999; Komatitsch et al., 1999). The SEM is a highly accurate  
 172 numerical method, which combines the geometrical flexibility of the finite-element method  
 173 with the fast convergence associated with spectral techniques, and it has origins in com-  
 174 putational fluid dynamics (Patera, 1984). It uses a mesh of hexahedral finite elements  
 175 on which the wave field is represented in terms of high-degree Lagrange polynomials on  
 176 Gauss–Lobatto–Legendre interpolation points. SEM is more accurate than widely used  
 177 classical techniques such as the finite-difference method (Virieux, 1986; Olsen et al., 1997),  
 178 in particular for surface waves (Komatitsch & Tromp, 1999, 2002a), which play an im-  
 179 portant role in ground-motion seismology (Komatitsch, 2004).

180 SPECFEM3D Cartesian has very good accuracy and convergence properties (Maday  
 181 & Patera, 1989; Priolo et al., 1994). It is also very well suited to parallel implementa-  
 182 tion on supercomputers and clusters of CPUs or GPUs (Komatitsch et al., 2003, 2008;

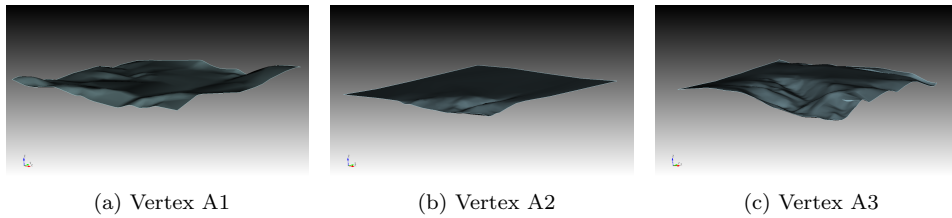


Figure 2: Elevation data at the three vertex locations of Einstein Telescope over areas with 3 km side lengths.

183 Tsuboi et al., 2003). SPEC3FEM3D software is written in Fortran2003 with full portability in mind (Komatitsch et al., 2018). The package uses the parallel algorithm based upon the Message Passing Interface (MPI) (Gropp et al., 1994; Pacheco, 1997).

186 We used Trelis for the creation of models and their exporting into a SPEC3FEM3D Cartesian file format. Trelis is a full-featured software for generation of two- and three-dimensional finite-element grids (meshes) and geometry preparation (Blacker et al., 2019). 187 188 189 Generating meshes for complex model-based geometries requires a variety of tools and many of them in Trelis are completely automatic. In creating a load-balanced, partitioned mesh, it is needed to set up a hexahedral mesh, in which goes a large amount of work, 190 191 then to export that mesh into a SPEC3FEM3D Cartesian file format and to partition it for a chosen number of cores in SPEC3FEM3D. The next step is creating the distributed 192 193 databases in which all the missing information needed by the SEM solver are created. The final step is to run the solver (Komatitsch et al., 2018). Creating the databases and 194 195 running the solver in SPEC3FEM3D is done on parallel on a number of cores chosen while 196 197 partitioning.

### 198 3.1 Governing equations

For elastic materials, the displacement field  $\mathbf{s}(\mathbf{x}, t)$  produced by a seismic source is governed by the momentum equation

$$\rho \partial_t^2 \mathbf{s} = \nabla \cdot \mathbf{T} + \mathbf{f}, \quad (1)$$

where  $\rho$  denotes mass density,  $\mathbf{T}$  the stress tensor and  $\mathbf{f}$  the seismic source (in our case non-uniform noise sources). On the free surface, the traction vector must vanish:

$$\tilde{\mathbf{n}} \cdot \mathbf{T} = 0, \quad (2)$$

where  $\tilde{\mathbf{n}}$  denotes the unit outward normal on the surface. On boundaries between different elastic materials, both traction  $\tilde{\mathbf{n}} \cdot \mathbf{T}$  and displacement  $\mathbf{s}$  need to be continuous. The stress tensor  $\mathbf{T}$  is linearly related to the displacement gradient  $\nabla \mathbf{s}$  by Hooke's law, which in a pure elastic solid may be written in the form (Martin & Komatitsch, 2009):

$$\mathbf{T} = \mathbf{c} : \nabla \mathbf{s}, \quad (3)$$

199 where  $\mathbf{c}$  denotes the fourth-order elastic tensor that describes the elastic properties of the medium (Peter et al., 2011). 200

201 Besides earthquake simulations, SPEC3FEM3D Cartesian includes functionality for seismic noise tomography as well. It can perform noise cross-correlation simulations. At the end of noise cross-correlation simulations, two outputs are the most interesting: the 202 203 simulated ensemble cross-correlations and the so-called ensemble sensitivity kernels, which 204 205 quantify how much a correlation depends on properties of the ground medium throughout the model. Cross-correlations are generated based on a SEM (Komatitsch & Vilotte, 206

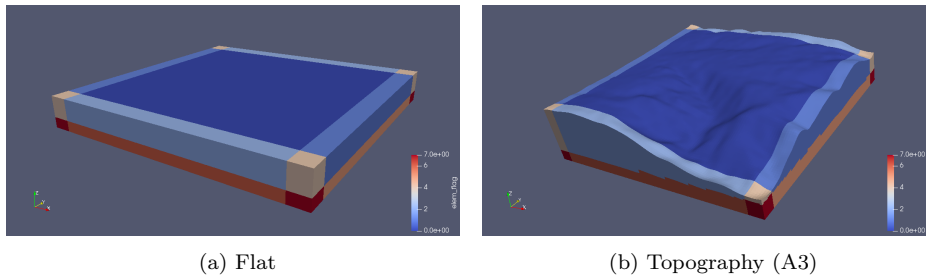


Figure 3: Models with convolutional perfectly matched boundary layers (C-PML).

1998; Komatitsch & Tromp, 1999) and ensemble finite-frequency sensitivity kernels are generated based on an adjoint method (Tromp et al., 2005; Liu & Tromp, 2008).

#### 4 Model setup

Before running simulations using created models, a time-consuming step is to set up appropriate absorbing boundary conditions. In order to simulate a semi-infinite medium, absorbing conditions are used on all sides of the model except the free surface. If absorbing boundary conditions are not good enough there are significant artificial boundary reflections from the numerical model which affect cross-correlations. The convolutional perfectly matched layers (C-PML) absorbing boundary condition is very efficient from a numerical point of view for the elastic-wave equation in absorbing body waves with non-grazing incidence and surface waves (Komatitsch & Martin, 2007). C-PML has better absorbing efficiency, especially in the case of small mesh size, than commonly used Clayton-Enquist absorbing boundary conditions which are mostly sufficient in the case of large mesh size (Komatitsch, 2004).

In order to create quality absorbing boundary layers out of the edge elements/layers of the meshed model, it is important to have those elements/layers as regular as possible with constant thickness and aligned with the coordinate grid axes (X, Y and/or Z). The thickness of C-PMLs can be different for the X, Y and Z sides, but must have a fixed, specific value for each coordinate individually. Usually, three or four C-PMLs on each of five absorbing model surfaces are sufficient, but as simulations showed, having more C-PMLs on each of the absorbing surfaces suppressed reflections more, regardless of the thickness of the single C-PML. A C-PML is very efficient but it does not absorb incident waves completely (see figure 7). In order to prevent remaining parasitic waves to affect cross-correlations i. e. to reach receivers, simulation time is set to be quite low (0.94 s). The thickness of the overall C-PML used for the flat surface model is 210 m, 210 m, 120 m for the X, Y and Z boundary planes, respectively (figure 3a), and for the topography model 179 m, 174 m, 179 m (figure 3b). More information about C-PML can be found in (Martin & Komatitsch, 2009; Komatitsch & Martin, 2007; Martin et al., 2010; Xie et al., 2014).

The important parameter values of the model are  $v_p = 3500$  m/s compressional-wave speed,  $v_s = 2000$  m/s shear-wave speed, and  $\rho = 2750$  kg/m<sup>3</sup> for the uniform mass density based on the fact that at the suggested site, granite and partly schist prevail, and also based on recent geoseismic studies (Giunchi et al., 2020). The simulations were performed without attenuation and anisotropy. Attenuation is not implemented yet for noise cross-correlation simulations and anisotropy is not important in small-scale computations. C-PML absorbing boundary condition is only supported in CPU mode for now (so one cannot use GPUs). Using GPUs would, of course, make the running of sim-

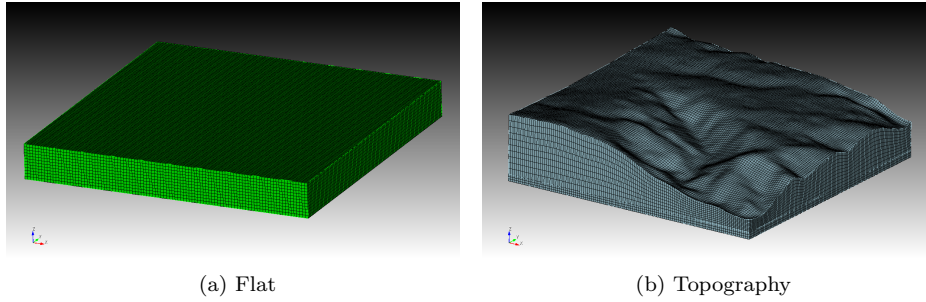


Figure 4: Meshed models.

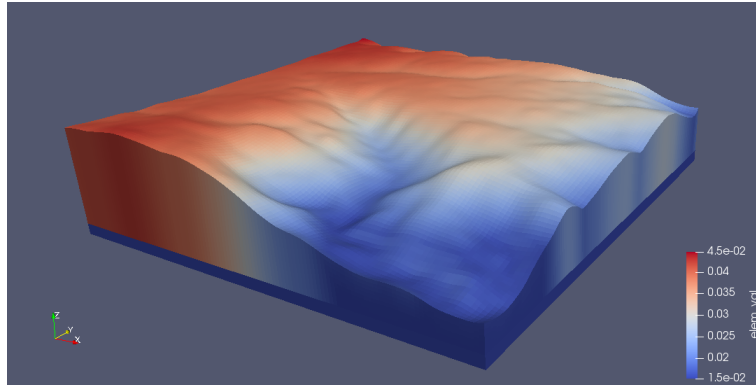


Figure 5: Minimum wave period resolved in each element of A3 topography model.

244 ulations much faster. Also, C-PML is still under test for the third step of cross-correlation  
 245 simulations – adjoint simulations.

246 The horizontal size of the models is  $3\text{ km} \times 3\text{ km}$  with a depth of 360 m in the flat  
 247 free surface case (figure 4a) and with variable depth in the case with A3 topography. The  
 248 minimum depth is 192 m and the maximum is 798 m (figure 4b). Mesh size of the flat  
 249 free surface model is 30 m (for all three dimensions). For the topography model, it varies  
 250 from 12 m to 71 m in Z dimension. For X and Y dimensions, it is 25 m.

251 Results of simulations are valid up to a certain maximum frequency (minimum pe-  
 252 riod). This maximum frequency depends on the mesh size and S-wave velocity and for  
 253 the flat, free surface model, it is 53 Hz (and it is constant throughout the model) and for  
 254 the topography model it varies between 22 Hz and 66 Hz. Minimum periods up to which  
 255 simulations at the A3 vertex are valid in specific mesh elements are shown for the to-  
 256 pography model in figure 5. The minimum period is an estimation, and there is no sharp  
 257 cut-off period for valid synthetics. Correlations become just more and more inaccurate  
 258 for periods shorter than this estimate. From what we saw from simulations, they are usu-  
 259 ally sufficiently accurate only up to about 10 Hz from estimated values, and this value  
 260 does not only depend on the mesh size and density, but also on details of the seismic-  
 261 source modeling.

262 Source distribution affects surface-waves amplitudes (Tsai & Moschetti, 2010), it  
 263 influences correlograms and its knowledge is important to correctly interpret the data  
 264 (Hanasoge et al., 2012; Basini et al., 2012). For cross-correlation simulations, the dis-  
 265 tribution of noise sources in SPECFEM3D Cartesian is constrained to the surface, which  
 266 is not a major drawback since the most relevant seismic sources in the NN band are ex-

267 pected to be surface sources. Also, we defined the ensemble of seismic sources used for  
 268 the cross-correlation simulation to have a minimum distance to the center of the model  
 269 surface since we assume that these areas will be protected in the future, i.e., excluding  
 270 the presence of strong seismic sources inside the protected area. The radius of this area  
 271 was also varied in our study to see the impact on seismic spectra and correlations.

## 272 5 Noise cross-correlation simulations

273 Ambient-noise seismology is of great relevance to high-resolution crustal imaging.  
 274 Thanks to the unprecedented dense data coverage, it affords in regions of little seismic-  
 275 ity (Basini et al., 2012). Cross-correlations between seismograms that recorded diffuse  
 276 seismic wavefields created by stochastic wave excitation at the Earth’s surface at differ-  
 277 ent seismographic stations show statistically significant signals to be present (Tromp et  
 278 al., 2010). A common interpretation of noise cross-correlations is to relate them to a form  
 279 of the Green’s function between two receivers (Wapenaar et al., 2006; Fan & Snieder,  
 280 2009).

The solution for boundary problems given by equation (1) can be expressed with  
 the help of Green’s tensor  $\mathbf{G}$

$$\mathbf{s}(\mathbf{x}, t) = \int_{-\infty}^t \int_{\Omega} \mathbf{G}(\mathbf{x}, \mathbf{x}'; t - t') \cdot \mathbf{f}(\mathbf{x}', t') d^3\mathbf{x}' dt'. \quad (4)$$

The Green’s tensor satisfies the relationship (Aki & Richards, 2009; Dahlen et al., 1998)

$$\mathbf{G}(\mathbf{x}, \mathbf{x}'; t - t') = \mathbf{G}^T(\mathbf{x}', \mathbf{x}; t - t'). \quad (5)$$

In frequency domain, the solution can be expressed using the Fourier transform

$$\mathbf{s}(\mathbf{x}, \omega) = \int_{\Omega} \mathbf{G}(\mathbf{x}, \mathbf{x}'; \omega) \cdot \mathbf{f}(\mathbf{x}', \omega) d^3\mathbf{x}'. \quad (6)$$

281 In practice, one uses an ‘ensemble average’ of many cross-correlations, which we will re-  
 282 fer to as the *ensemble cross-correlation*. One of the most important data-processing tech-  
 283 niques in all of the ambient-noise seismology is ensemble averaging, allowing to reduce  
 284 the effects of a set of scatterers and sources randomly distributed in time and space to  
 285 those of a diffuse wavefield (Basini et al., 2013). Ensemble-averaged cross-correlations  
 286 between synthetic seismograms at two geographically distinct locations on the free sur-  
 287 face are determined under the assumption that noise is spatially uncorrelated but non-  
 288 uniform. We focus our study on seismic surface measurements, despite the advantages  
 289 of deeper seismometer installations (Mandic et al., 2018).

Let us consider the  $\hat{\mathbf{v}}^\alpha$  component of the displacement at location  $\mathbf{x}^\alpha$ , and the  $\hat{\mathbf{v}}^\beta$   
 component of the displacement at location  $\mathbf{x}^\beta$ :

$$s^\alpha(t) \equiv \hat{\mathbf{v}}^\alpha \cdot \mathbf{s}(\mathbf{x}^\alpha, t), \quad s^\beta(t) \equiv \hat{\mathbf{v}}^\beta \cdot \mathbf{s}(\mathbf{x}^\beta, t) \quad (7)$$

The cross-correlation between those two time-series is given by

$$C^{\alpha\beta}(t) = \int s^\alpha(t + \tau) s^\beta(\tau) d\tau \quad (8)$$

We assume that sources of the field are spatially uncorrelated, which implies

$$\langle f_j(\mathbf{x}', t') f_m(\mathbf{x}'', t'') \rangle = S_{jm}(\mathbf{x}', t' - t'') \delta(\mathbf{x}' - \mathbf{x}'') \quad (9)$$

290 where  $\langle \cdot \rangle$  denotes an ensemble average (Woodard, 1997).  $S_{jm}$  describes the geographic  
 291 and geometric properties and  $\omega$ -dependence of the noise sources, it is non-zero only at  
 292 the (surface) locations of the seismic sources.

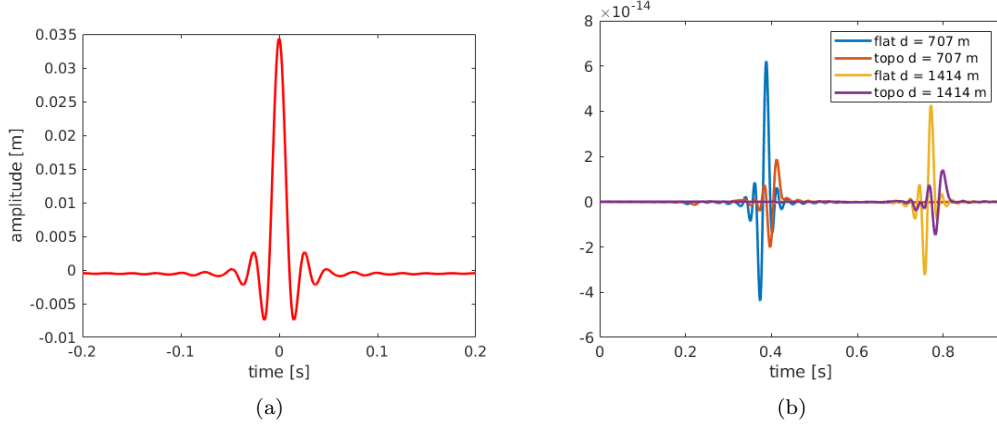


Figure 6: Source time function corresponding to the noise spectrum (a) and vertical displacement of generating wavefield at two locations (b).

Using Fourier transform, a representation in terms of the Green’s tensor, and taking into consideration ensemble average and equation (5), the analytical expression for ensemble cross-correlation is:

$$\langle C^{\alpha\beta} \rangle (t) = \frac{1}{2\pi} \hat{v}_i^\alpha \hat{v}_\ell^\beta \iint S_{jm}(\mathbf{x}, \omega) G_{ji}(\mathbf{x}, \mathbf{x}^\alpha; \omega) G_{m\ell}^*(\mathbf{x}, \mathbf{x}^\beta; \omega) \exp(i\omega t) d^3\mathbf{x} d\omega. \quad (10)$$

One may notice that ensemble cross-correlations have the symmetry:

$$\langle C^{\alpha\beta} \rangle (t) = \langle C^{\beta\alpha} \rangle (-t). \quad (11)$$

The more detailed calculation can be found in (Tromp et al., 2010).

Our noise cross-correlation simulations require two steps. In the first step, one calculates a generating wavefield obtained by inserting a source time function at the location of the first receiver. The source time function of the generating wavefield is obtained using the spectrum of the ensemble-averaged noise, and it is narrowly concentrated around zero time (figure 6a). In these simulations, a noise spectrum is used that is flat in the interesting frequency range (1 – 30 Hz). Results can be rescaled using realistic / observed seismic spectra when needed. Then, the results of the generating wavefield are saved at each time step at locations where the actual noise sources are located, which in our simulation covers an area of the free surface. Displacement in the vertical direction of the generating wavefield for the flat and topography models at two locations with different distances from the source are shown in figure 6b.

Next, in the second step, one uses this generating wavefield at the locations of the noise sources as sources of the ensemble forward wavefield associated with the first receiver. We assume that the excitation is along the vertical direction of the surface. In the case of vertical forces, more than two thirds of the total energy is radiated as Rayleigh waves (Woods, 1968). Regarding our application, at the surface, the relative amount of Rayleigh waves is even larger (Sanchez-Sesma & Campillo, 1991). It should also be noted that in our models, which basically represent a homogeneous halfspace, no other modes of Rayleigh waves, apart from the fundamental Rayleigh mode, are possible. The source of the ensemble forward wavefield is just the time-reversed generating wavefield. The ensemble cross-correlation is equal to the  $\hat{v}^\alpha$  component of the ensemble forward wavefield  $\Phi^\beta$  evaluated at location  $\mathbf{x}^\alpha$ :

$$\langle C^{\alpha\beta} \rangle (t) = \hat{v}^\alpha \cdot \Phi^\beta(\mathbf{x}^\alpha, t). \quad (12)$$

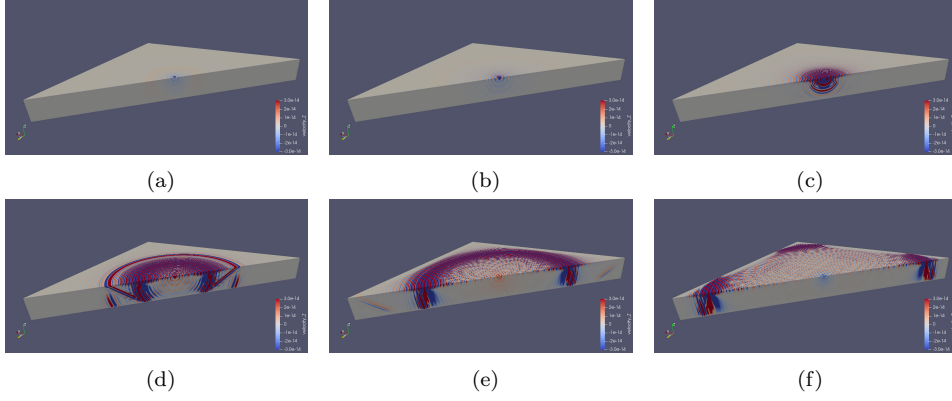


Figure 7: Propagation of seismic waves for the flat surface model using a source time function determined by the spectrum of the ensemble-averaged noise.

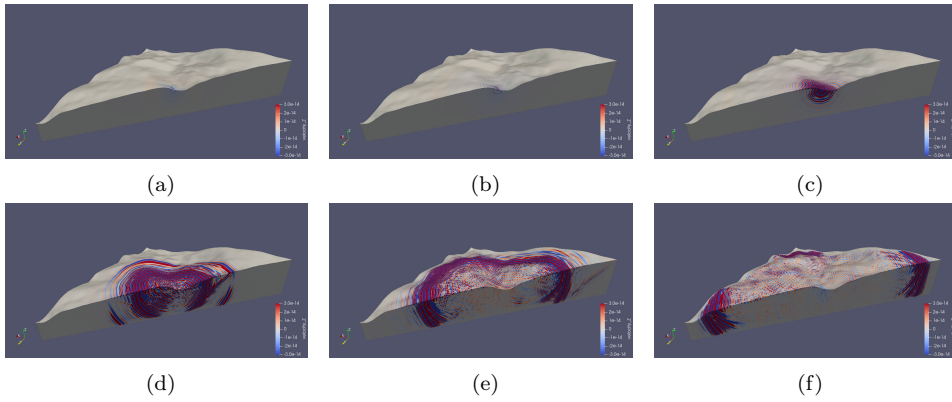


Figure 8: Propagation of seismic waves for the A3 topography model using a source time function determined by the spectrum of the ensemble-averaged noise.

305 Having in mind equation (11), it is clear that knowing either  $\Phi^\alpha$  or  $\Phi^\beta$  the ensemble cross-  
 306 correlation can be calculated. More details can be found in (Tromp et al., 2010). A se-  
 307 quence of snapshots resulting from a simulation of the wavefield with a source at the center  
 308 of the model surface with the source time function as in figure 6a can be seen in fig-  
 309 ure 7 for the flat model and in figure 8 for the A3 topography model.

## 310 6 Sensitivity kernels

311 Another step can be taken with noise cross-correlation simulations to obtain sensi-  
 312 tivity kernels, which quantify the sensitivity of the cross-correlations to parameters of  
 313 the ground medium such as mass density and seismic speeds. In addition to the gener-  
 314 ating and ensemble forward wavefield described in section 5, the calculation of sensiti-  
 315 vity kernels requires another wavefield called ensemble adjoint wavefield. The sensitivity  
 316 kernel results from an interaction between the ensemble forward wavefield and the en-  
 317 semble adjoint wavefield. It is then possible to estimate sensitivity kernels without re-  
 318 quiring computationally expensive ensemble averages as done in practice when analyz-  
 319 ing seismic data (substituting ensemble averages by temporal averages). As a technical  
 320 note, the calculation of sensitivity kernels with SPECFEM3D does not currently sup-  
 321 port C-PML. We used Clayton-Enquist boundary conditions for these simulations.

322 In seismology, sensitivity kernels are very important for tomographic inversion and  
 323 can be used to improve Earth and source models. They illuminate those parts of mod-  
 324 els that are inaccurate. In other words, using observed correlations and making simu-  
 325 lations of synthetic correlations, one uses the cross-correlation misfit to iteratively im-  
 326 prove the model. More about ensemble adjoint wavefield and sensitivity kernels can be  
 327 found in (Liu & Tromp, 2006; Tromp et al., 2005; Tromp et al., 2008; Tromp et al., 2010;  
 328 Peter et al., 2011). Sensitivity kernels are not of direct relevance to our work, but they  
 329 give additional information whether the model size is sufficiently large for the simula-  
 330 tion of correlations, in which case sensitivity kernels should be small towards the bound-  
 331 aries of the model. For the future, they can guide the development of more sophisticated  
 332 models with inhomogeneous geology.

333 The theoretical work in (Tromp et al., 2010) shows how adjoint techniques (e.g. (Tromp  
 334 et al., 2005; Peter et al., 2007)) can be applied to ambient-noise seismology taking into  
 335 account the non-uniform distribution of noise sources. The ensemble adjoint wavefield  
 336 is produced by a source located at the second receiver whose time function depends on  
 337 the misfit between simulated and observed correlations. There are various possibilities  
 338 to evaluate cross-correlation misfits. The method chosen in SPECFEM3D is based on  
 339 the misfit of cross-correlation delay times. The cross-correlation delay time would for ex-  
 340 ample be responsible for a complex phase of cross-spectral densities between sensors. Since  
 341 we are only interested in the sensitivity kernel and not in the actual inference of ground  
 342 properties using seismic observations, an arbitrary misfit of  $\Delta T = 1$  s is chosen (Tromp  
 343 et al., 2010).

344 The ensemble adjoint source corresponding to a delay-time misfit involves the first  
 345 time derivative of the simulated ensemble cross-correlation  $\langle \dot{C}^{\alpha\beta} \rangle$ . As will be shown sub-  
 346 sequently, ensemble cross-correlations are dominated by Rayleigh surface waves, whose  
 347 main sensitivity is to shear-wave speed (often given the symbol  $\beta$ ). So here, we focus on  
 348 beta kernels. The beta kernel is a volumetric field representing the gradient of the mis-  
 349 fit function with respect to S-wave speed.

350 The beta kernel is shown in figure 9 for the flat (top) and for the A3 topography  
 351 model (bottom). One can see that cross-correlations are most sensitive to properties of  
 352 the ground close to and between the two receivers and close to the surface. Note that  
 353 the kernel is asymmetric with respect to an exchange of receivers. This asymmetry comes  
 354 from the fact that kernels are defined for two branches, the so-called positive and neg-  
 355 ative branch (the positive branch being shown). The positive branch describes cross-correlations  
 356 whose time delays are consistent with waves reaching the second receiver before the first.

357 If we interpreted the 1 s time delay as an observed misfit, then the plots in figure  
 358 9 would tell us that the S-wave speed in the region between the two receivers, since the  
 359 kernel is negative here, would have to be decreased to reduce the time-delay misfit be-  
 360 tween observation and model. The sign of the kernel would be inverted in the negative  
 361 branch since the model would have to be corrected to increase a negative time delay.

## 362 7 Results

363 Einstein Telescope targets GW observations down to a few Hertz (Punturo et al.,  
 364 2010), which means that seismic NN will play an important role for instrument design.  
 365 The detector will be hosted in an underground infrastructure, which creates a low-noise  
 366 environment providing an essential reduction of NN. Detector infrastructure including  
 367 pumps and ventilation must not disturb the underground environment or be at a safe  
 368 distance to the test masses. Further mitigation of NN can be achieved by noise cancel-  
 369 lation using an extensive monitoring system of the ambient seismic field (Harms, 2019).  
 370 The idea is to pass seismic data through a filter such that its output can be understood  
 371 as a coherent estimate of seismic NN and be subtracted from the GW data (Cella, 2000).

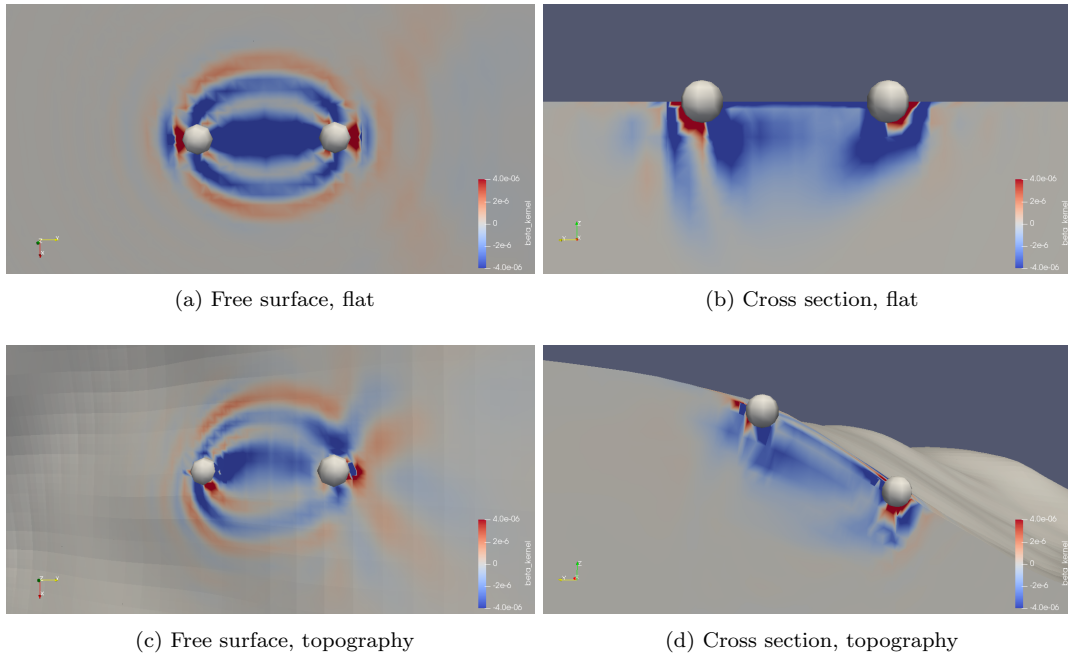


Figure 9: Beta kernel for flat (top row) and topography surface model (bottom row). White spheres represent receivers at a distance of 130 m from each other.

372 These filters can take the form of Wiener filters calculated from the correlations between  
 373 seismometers and the GW detector. The most challenging aspect of this technology is  
 374 to determine the locations of a given number of sensors that optimize the cancellation  
 375 performance (Coughlin et al., 2016; Badaracco & Harms, 2019).

376 Rayleigh waves are predicted to give the dominant contribution to NN in surface  
 377 detectors (Coughlin et al., 2016; Harms et al., 2020) and even underground detectors can  
 378 still be limited by gravitational noise from Rayleigh waves depending on the detector depth  
 379 (Badaracco & Harms, 2019). The Rayleigh field produces surface displacement and den-  
 380 sity perturbations beneath the surface at the same time (Hughes & Thorne, 1998; Bec-  
 381 caria et al., 1998), which leads to gravity perturbations. Even if we do not know the wave  
 382 composition of a seismic field at a site, it is still reasonable in many cases to assume that  
 383 Rayleigh waves dominate the normal surface displacement at frequencies in the range  
 384 1 Hz – 20 Hz produced by surface or near-surface seismic sources (Mooney, 1976; Bonnefoy-  
 385 Claudet et al., 2006). Only at exceptionally quiet (necessarily remote) surface sites or  
 386 underground sites, body-wave content is expected to be significant or dominant in this  
 387 band (however, mode content can change significantly with time if due to natural sources  
 388 (Coughlin et al., 2019)).

389 In the following, we present results of our analyses of spatial correlations in an ambi-  
 390 ent seismic field simulated with SPEC3D, and we predict the correlation between  
 391 surface seismometers and the gravity perturbation experienced by an underground test  
 392 mass, which is the crucial information for the optimization of surface arrays for NN can-  
 393 cellation. As will be explained, our analyses are constrained by the computational re-  
 394 sources that were available to us. One consequence is that it was not possible to run a  
 395 simulation with a test-mass depth greater than 100 m (while 200 m – 300 m is the envi-  
 396 sioned depth of ET test masses), since this would have required a dense set of receivers  
 397 distributed over a much larger surface area. We learn from these results how topogra-

398 phy impacts correlations, which we expect to be the main site effect on seismic corre-  
 399 lations and seismic gravitational noise.

## 400 7.1 Seismic scattering

401 The effect of scattering of seismic waves from surface topography on seismic cor-  
 402 relation and gravity perturbations of test masses needs to be quantified using the meth-  
 403 ods outlined in section 5. As mentioned earlier, because of the way we choose to excite  
 404 seismic waves in this analysis, the ensemble forward field is mainly composed of Rayleigh  
 405 surface waves. For flat, free surfaces, Rayleigh waves, once decoupled from the near field  
 406 of the seismic sources, propagate without conversion into other seismic modes.

407 The scattering by topography depends on the size of elevation changes, area of con-  
 408 tact, and the length scale of the irregularity. It also depends significantly on incident an-  
 409 gle and type of seismic waves propagating through the area. Amplitudes of scattered waves  
 410 should increase linearly with the size of elevation changes for small obstacles according  
 411 to perturbation theory calculations. The scattering should be much reduced in the case  
 412 of irregularities with gentle curvature when compared with irregularities (mountains) with  
 413 abrupt discontinuities in curvature (bluff topography) (Gilbert & Knopoff, 1960). An  
 414 important point is that the incident wave is essentially "blind" to features that are much  
 415 smaller than a wavelength (Otto, 1977). Scattering always becomes weaker at smaller  
 416 frequencies if all other parameters are kept constant, but generally, there is no simple  
 417 frequency scaling valid for the entire wavenumber space. Scattering coefficients in wavenum-  
 418 ber space are mainly proportional to the topographic spectrum (Coughlin & Harms, 2012).  
 419 The maximum scattering is generally present when seismic wavenumbers match the wavenum-  
 420 bers of the topographic spectrum (J. Hudson & Knopoff, 1967).

421 In our ensemble forward wavefield, there is also body-wave content. So, it is inter-  
 422 esting to see what happens with body waves during scattering in addition to the dom-  
 423 inant Rayleigh-wave field. In the case of incident S-waves, if the dominant horizontal length  
 424 scales of the surface spectrum are small compared with the length of incident waves, the  
 425 amplitudes of some of the scattered waves decrease exponentially with depth similar to  
 426 Rayleigh waves. A periodic surface characterized by short horizontal length scales traps  
 427 more of the incident energy than one characterized by longer length scales, but the amount  
 428 of trapped energy also depends on the associated amplitudes of the topographic spec-  
 429 trum. This trapped energy feeds into the surface waves (Abubakar, 1962).

430 For the incident P-waves, scattered waves are mostly Rayleigh waves accompanied  
 431 by a weaker (horizontal) P-wave (Bard, 1982). The amplitude ratio of scattered Rayleigh  
 432 to incident longitudinal wave depends mostly on angle of incidence and horizontal and  
 433 vertical dimension of the corrugation. For example, for normally incident longitudinal  
 434 waves, with Rayleigh wavelength equal to the width of corrugation, amplitude ratio grows  
 435 linearly with ratio of horizontal and vertical dimensions of the corrugation. Already at  
 436 ratios of horizontal and vertical dimensions less than one, scattered Rayleigh wave has  
 437 surface amplitude that is greater than that of the incident longitudinal wave alone (Hudson  
 438 et al., 1973). In conclusion, a significant percentage of bulk waves scatter into Rayleigh  
 439 waves and additionally that scattering is driven by high-wavenumber components of the  
 440 surface topography, which typically have weaker amplitudes.

441 For incident Rayleigh waves, which is the most interesting case for us, scattering  
 442 effects were investigated in (Maradudin & Mills, 1976). The main conclusion that one  
 443 may draw from there is that the predominant contribution from the roughness-induced  
 444 scattering of the incident Rayleigh wave is into other Rayleigh waves. At low frequen-  
 445 cies, the ratio between scattered Rayleigh and bulk waves is about 10, and it grows as  
 446 the frequency increases. So Rayleigh wave/Rayleigh wave scattering contribution is about  
 447 an order of magnitude larger than the bulk wave contributions. However, details depend  
 448 on the topography.

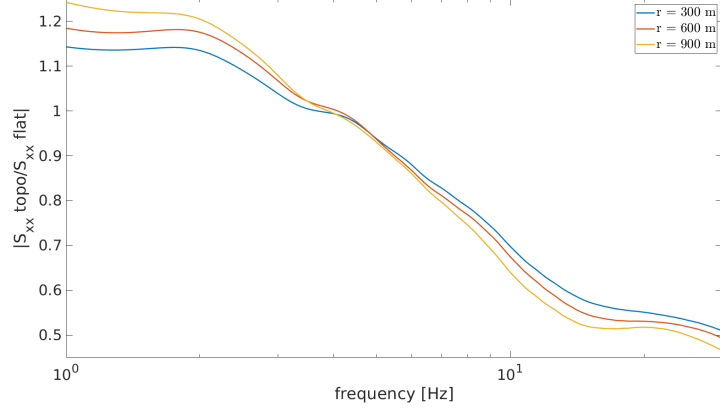


Figure 10: Ratio of seismic spectral densities at the center of topographic (A3 vertex) and flat models for different values of the minimal distance of seismic sources.

449 Scattering especially from Rayleigh waves into Rayleigh waves is a very efficient  
 450 scattering channel, but since it does not cause a change in wave type, its impact on NN  
 451 cancellation can easily be modeled. Still, it is found that topographic scattering might  
 452 be relevant to NN subtraction in regions with rough topography (Coughlin & Harms,  
 453 2012). Fields of scattered waves do not generally permit a unique correspondence be-  
 454 tween frequency and wavelength, since at each frequency, the wavenumber spectrum of  
 455 the scattered field is typically continuous. This is the main challenge for the design of  
 456 a NN cancellation system in seismic fields with significant contributions from scattered  
 457 waves. We need to mention that also scattering from underground caverns of the Ein-  
 458 stein Telescope would significantly modify the seismic field in the vicinity of the cavern,  
 459 but the impact on NN remains small as long as the caverns are much smaller than the  
 460 seismic wavelengths in the relevant frequency range (Harms, 2019).

461 As a first characterization of topographic scattering, we calculate the ratio of power  
 462 spectral densities at the center of our models with and without topography. The ratio  
 463 is shown in figure 10 between 1 Hz and 30 Hz for three different minimal distances of seis-  
 464 mic sources to the center point. The plot shows that higher frequencies are more scat-  
 465 tered out with respect to lower frequencies by topography. In other words, topography  
 466 acts as a low-pass for Rayleigh waves protecting a point to some extent from the influ-  
 467 ence of distant seismic sources. At the A3 vertex of the Einstein Telescope, topographic  
 468 protection is provided down to about 4 Hz. As can be seen, the ratio depends weakly on  
 469 the minimal distance of seismic sources, which can be explained by the contribution of  
 470 increasingly large topographic scales to the scattering coefficients. Of course, the abso-  
 471 lute value of power spectral density reduces significantly when sources are more distant.  
 472

## 473 7.2 Seismic coherence

The SPEC-FEM3D simulation of seismic correlations yields a time-domain correlation  $C_{ij}(\tau)$  between two receivers. For our analysis, we need the Fourier transform,

$$S_{ij}(f) = \int_{-\infty}^{\infty} d\tau C_{ij}(\tau) e^{i2\pi f\tau}, \quad (13)$$

which, according to the Wiener-Khinchin theorem, is the cross power-spectral density (CPSD) between the two sensors. The CPSD can be normalized so that its absolute value

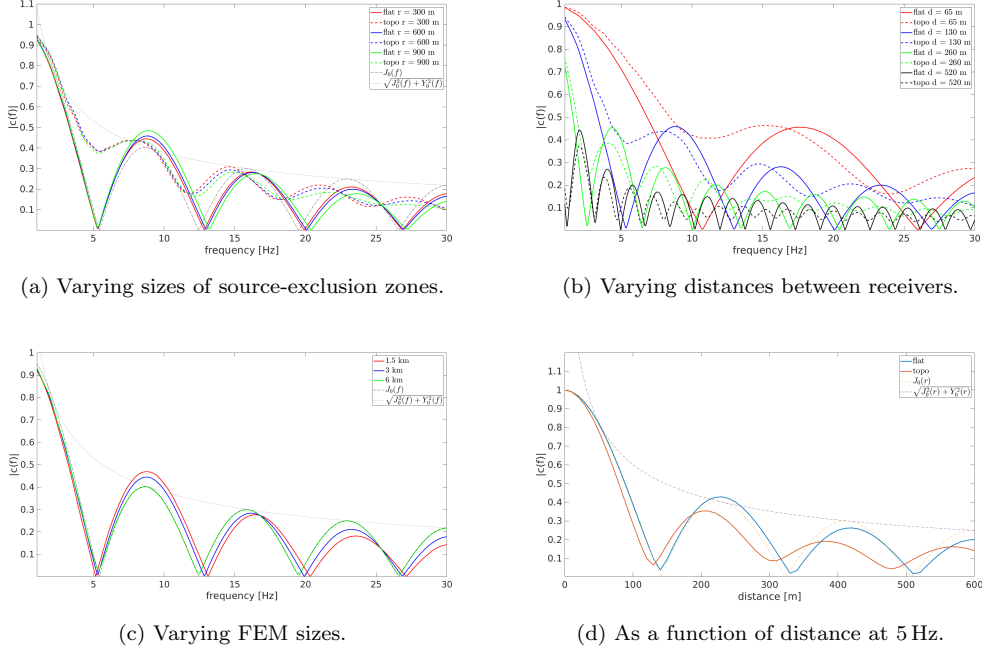


Figure 11: Plots of seismic coherence calculated by SPEC3FEM3D.

lies between 0 and 1, a quantity called *coherence*:

$$c_{ij}(f) = \frac{S_{ij}(f)}{\sqrt{S_i(f)S_j(f)}}. \quad (14)$$

Figure 11 summarizes four analyses of seismic coherence with SPEC3FEM3D. In plot (a), we show the absolute value of coherence for the flat-surface and A3-topography models with varying minimal distances of seismic sources of the ambient field. While the coherence is significantly different between the two models, it only depends weakly on the minimal distance of sources. The plot also contains an analytical prediction of coherence for the flat-surface, isotropic Rayleigh-wave field, where the coherence is given by a Bessel function

$$c_{ij}(f) = J_0(2\pi f|\vec{r}_j - \vec{r}_i|/c) \quad (15)$$

with a Rayleigh-wave speed of  $c = 1840$  m/s. In this simple case, the coherence is real-valued, but it is generally a complex quantity. The distance between the two receivers is 130 m.

Plot (b) displays the absolute value of coherence for varying distance between the two receivers. Again, the coherence obtained from the A3-topographic model is qualitatively different from the flat-surface coherence for all distances between receivers. With the A3-topographic model,  $|c_{ij}(f)|$  does not vanish at any frequency, which is likely due to a mixed wave content with Rayleigh waves and scattered waves of different wavelengths.

In plot (c), we verify that the size of the standard finite-element model ( $3 \text{ km} \times 3 \text{ km}$ ) was not chosen too small for analyses in this paper, i.e., that coherence changes weakly when increasing model size. While some change in coherence can be observed, it is minor especially in the frequency band of interest 3 Hz – 10 Hz, where NN might limit the sensitivity of Einstein Telescope.

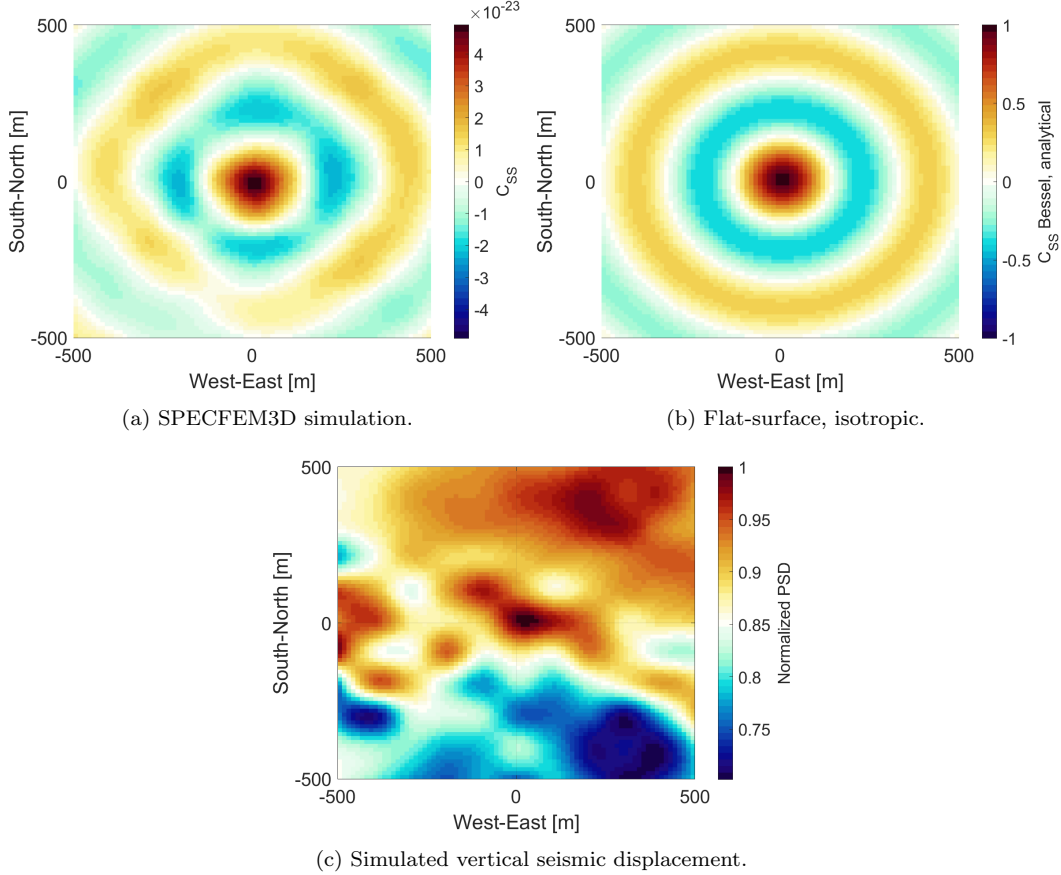


Figure 12: Correlations (a) and spectral densities (c) calculated for an ambient field with SPECFEM3D at 5 Hz. The ideal seismic correlations in the case of a flat surface and isotropic field is shown in (b).

487 Finally, in plot (d),  $|c_{ij}(f)|$  is shown as a function of distance at frequency 5 Hz.  
 488 The aforementioned qualitative difference between the flat-surface and A3-topographic  
 489 models can be seen again. The flat-surface model closely follows the analytical model  
 490 of an isotropic, flat-surface Rayleigh-wave field.

491 **7.3 Gravity-displacement correlation**

492 It is possible to express the gravity perturbation produced by a seismic field in terms  
 493 of an integral over seismic correlations (Harms, 2019). It is possible to separate contri-  
 494 butions from compression and decompression of the ground medium by seismic waves  
 495 and from surface displacement. Surface displacement is typically much stronger than un-  
 496 derground displacement due to the presence of surface waves such as Rayleigh waves. One  
 497 of the reasons why Einstein Telescope is proposed as underground infrastructure is to  
 498 avoid the relatively strong gravitational noise from surface displacement (Amann et al.,  
 499 2020).

As a consequence, and as a first step, we attempt to model the gravitational coupling between seismic surface fields and underground gravitational perturbations. The

equation to be used takes the form of a surface integral (Harms, 2019)

$$C(\delta a_{\text{arm}}(\mathbf{r}_0), \xi_z(\mathbf{r}); f) = G\rho_0 \int d^2\mathbf{r}' C(\xi_n(\mathbf{r}'), \xi_z(\mathbf{r}); f) \frac{(\mathbf{r}' - \mathbf{r}_0) \cdot \mathbf{e}_{\text{arm}}}{|\mathbf{r}' - \mathbf{r}_0|^3}, \quad (16)$$

500 which is the CPSD between vertical seismic displacement  $\xi_z$  monitored at  $\mathbf{r}$  and hori-  
 501 zontal gravitational acceleration  $\delta a_{\text{arm}}$  at the location  $\mathbf{r}_0$  of an underground test mass.  
 502 Here,  $G$  is Newton's gravitational constant,  $\rho_0$  is the mass density of a homogeneous ground,  
 503 and  $\mathbf{e}_{\text{arm}}$  is the unit vector pointing along the detector arm of Einstein Telescope. The  
 504 integral contains the CPSD between vertical and normal surface displacement provided  
 505 by SPEC-FEM3D simulations. We focus on vertical surface displacement since it is typi-  
 506 cally associated with Rayleigh waves while horizontal displacement can have important  
 507 contributions from Love waves. Since a homogeneous medium is simulated here, Love  
 508 waves do not play a role, but it is still convenient for practical reasons (when compar-  
 509 ing with other work or seismic observations) to focus on vertical displacement.

510 The seismic CPSD  $C(\xi_n(\mathbf{r}' = \mathbf{0}), \xi_z(\mathbf{r}); f)$  for the A3-topographic model is shown  
 511 in plot (a) of figure 12. It only represents a small subset of all seismic correlations re-  
 512 quired for equation (16). The result can be compared with the seismic CPSD in the case  
 513 of a flat-surface, isotropic Rayleigh wave field shown in plot (b). Topography has a sig-  
 514 nificant impact on seismic correlations, but the pattern of concentric rings is approxi-  
 515 mately preserved. The third plot shows the variation of power spectral densities of ver-  
 516 tical surface displacement. Again, topography leaves a clear imprint on the seismic field  
 517 in the form of an inhomogeneity.

Equation (16) can be solved analytically in the case of a flat-surface, isotropic Rayleigh  
 field, which yields (Harms, 2019):

$$C(\delta a_{\text{arm}}(\mathbf{0}), \xi_z(\mathbf{r}); f) = 2\pi G\rho_0 S(\xi_z; f) e^{-hk(f)} \cos(\phi) J_1(k(f)r), \quad (17)$$

518 with  $\mathbf{r} = (r \cos(\phi), r \sin(\phi), h)$ ,  $\phi$  being the angle between detector arm and the hori-  
 519 zontal projection of  $\mathbf{r}$ , and  $k(f)$  is the wavenumber of plane Rayleigh waves. According  
 520 to this model, the CPSD between vertical displacement and gravity perturbation van-  
 521 ishes for  $\mathbf{r} = \mathbf{0}$ . It is shown in plot (a) of figure 13. Instead, plot (b) is calculated by  
 522 inserting the isotropic, flat-surface correlation of equation (15) into equation (16), but  
 523 with a kernel that depends on topography. This shows that the kernel has an important  
 524 impact on the seismic-gravitational CPSD, e.g., the nodal line along the south-north di-  
 525 rection seen in plot (a) is not present in plot (b). Finally, the seismic-gravitational CPSD  
 526 calculated with the seismic CPSD from SPEC-FEM3D and topographic kernel in equa-  
 527 tion (16) is shown in plot (c).

The result in plot (d) tells us where a single seismometer should be placed to ob-  
 tain the best reduction of NN by coherent cancellation with a Wiener filter. The plot-  
 ted quantity is

$$S(w; f) = |C(\delta a_{\text{arm}}(\mathbf{r}_0), \xi_z(\mathbf{r}); f)|^2 / C(\xi_z(\mathbf{r}), \xi_z(\mathbf{r}); f), \quad (18)$$

528 which is the power spectral density of the output of the Wiener filter (Cella, 2000; Harms,  
 529 2019). The higher it is, the more NN the Wiener filter is able to cancel in the data of  
 530 the Einstein Telescope. This optimal placement of a seismometer is at (-38 m, -113 m).  
 531 The problem gets significantly more complicated if one wants to deploy multiple seis-  
 532 mometers since the placement of sensors also depends on their mutual CPSDs (Badaracco  
 533 & Harms, 2019). Nonetheless, the quantities required for such a multi-sensor optimiza-  
 534 tion are provided by SPEC-FEM3D. They need to be used in numerical optimization rou-  
 535 tines. What we in fact propose is to use the correlation results from numerical analy-  
 536 sis as presented in this paper to define priors for a Gaussian Process Regression, which  
 537 then combines priors and observed seismic correlations for a Bayesian inference of seis-  
 538 mic correlations everywhere in the medium, which forms the basis of the optimization  
 539 algorithm (Badaracco et al., 2020).

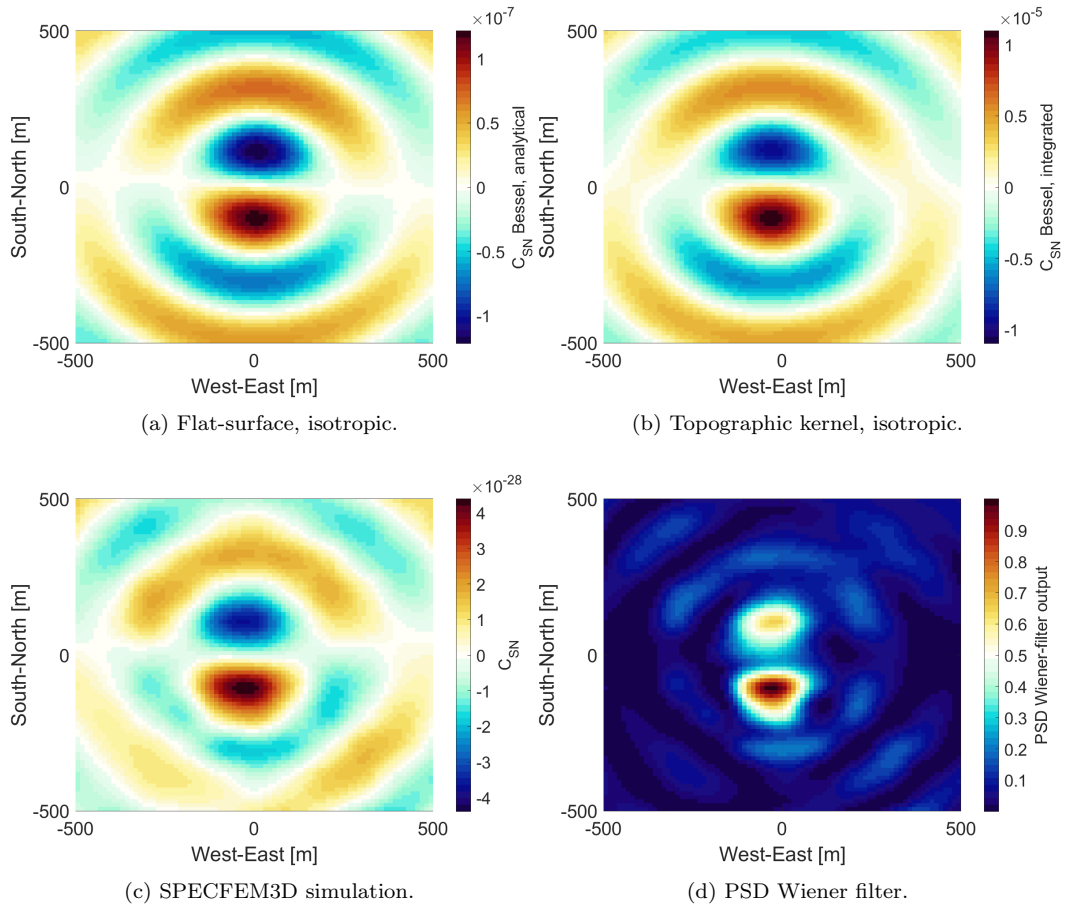


Figure 13: Seismic-gravitational correlations of an ambient field at 5 Hz (a) – (c). The normalized PSD of the Wiener-filter output is shown in (d). The test mass is located 100 m underground. The direction of gravity acceleration is along the A3 – A1 detector arm.

## 8 Conclusion

In this paper, we presented synthetic seismic and gravitoelastic correlations between seismometers and a suspended underground test mass as part of the next-generation, gravitational-wave detector Einstein Telescope. The synthetics were calculated with the spectral-element SPECFEM3D Cartesian software. The main analysis was based on a topographic model centered at one of the vertices (A3) at a candidate site in Sardinia of the Einstein Telescope.

We found that A3 topography has generally a significant impact on seismic and gravitoelastic correlations. Specifically, calculations showed that Sardinian topography at vertex A3 scatters out energy from Rayleigh waves above 4 Hz providing protection from the influence of distant seismic sources. As expected, symmetries of the field of gravitoelastic correlations are broken by topography leading to unique solutions of optimal seismometer placement for gravity-noise cancellation.

The results are a powerful demonstration of SPECFEM3D’s capability to model correlations in ambient seismic fields for the purpose of designing noise-cancellation systems using seismometer arrays. We proposed to use the numerical results to define priors of a Gaussian Process Regression, which includes seismic observations to infer gravitoelastic correlations throughout the entire ground medium. This is a crucial step to calculate optimal array configurations for gravity-noise cancellation, which we expect to require several tens to hundreds of seismometers deployed in boreholes around 12 of the test masses of the Einstein Telescope.

Since this work only addressed gravity perturbations from seismic surface displacement, an important future task is to extend the analysis to gravity perturbations resulting from (de)compression of rock by seismic waves, and from displacement of underground cavern walls. In addition, geological inhomogeneities may be significant, which means that they should also be included in future modeling. Current understanding of geology near the three vertex locations can be improved by drill-core and geoseismic studies, which would help to build a more accurate model and to improve simulation results.

## Acknowledgments

To prepare the topography data one can get SRTM Digital Elevation Data for a region of interest at: <http://srtm.csi.cgiar.org>. Besides, this is a modeling and simulation paper. There is no data necessary to understand, evaluate, or replicate our results. It is all based on creating a model and running the simulations on it, which anyone can repeat in principle with the information in the paper. SPECFEM3D is maintained by the Computational Infrastructure for Geodynamics (<http://geodynamics.org>), which is funded by the National Science Foundation under awards EAR-0949446 and EAR-1550901. The work was supported by the PRIN project “Characterization of the Sos Enattos mine in Sardinia as the site for the Einstein Telescope GW observatory”. We thank the Sardinia site-study team for useful discussions and suggestions for this manuscript. We acknowledge the usage of the high-performance cluster at CNAF, the central computing facility of INFN at Bologna. We are grateful for the continuous support we received from its staff.

## References

- Abbott, B. P., Abbott, R., Abbott, T. D., Abernathy, M. R., Acernese, F., Ackley, K., . . . Zweigig, J. (2016, March). GW150914: The Advanced LIGO Detectors in the Era of First Discoveries. *Physical Review Letters*, *116*, 131103. Retrieved from <http://link.aps.org/doi/10.1103/PhysRevLett.116.131103>  
doi: 10.1103/PhysRevLett.116.131103
- Abubakar, I. (1962, January). Scattering of plane elastic waves at rough sur-

- 589 faces. I. *Mathematical Proceedings of the Cambridge Philosophical So-*  
590 *ciety*, 58, 136–157. Retrieved from [http://journals.cambridge.org/](http://journals.cambridge.org/article/S030500410003629X)  
591 [article/S030500410003629X](http://journals.cambridge.org/article/S030500410003629X) doi: 10.1017/S030500410003629X
- 592 Abubakar, I. (1963, January). Scattering of plane elastic waves at rough surfaces.  
593 ii. *Mathematical Proceedings of the Cambridge Philosophical Society*, 59, 231 –  
594 248. doi: 10.1017/S0305004100002176
- 595 Acernese, F., Agathos, M., Agatsuma, K., Aisa, D., Allemandou, N., Allocca, A.,  
596 ... others (2015). Advanced Virgo: a second-generation interferometric  
597 gravitational wave detector. *Classical and Quantum Gravity*, 32(2), 024001.  
598 Retrieved from <http://stacks.iop.org/0264-9381/32/i=2/a=024001> doi:  
599 10.1088/0264-9381/32/2/024001
- 600 Acernese, F., Antonucci, F., Aoudia, S., Arun, K., Astone, P., Ballardin, G., ...  
601 Yvert, M. (2010). Measurements of Superattenuator seismic isolation by  
602 Virgo interferometer. *Astroparticle Physics*, 33(3), 182 - 189. Retrieved from  
603 <http://www.sciencedirect.com/science/article/pii/S0927650510000253>  
604 doi: <http://dx.doi.org/10.1016/j.astropartphys.2010.01.006>
- 605 Aki, K., & Richards, P. G. (2009). *Quantitative Seismology, 2nd edition*. University  
606 Science Books.
- 607 Akutsu, T., et al. (2019). KAGRA: 2.5 Generation Interferometric Gravitational  
608 Wave Detector. *Nature Astronomy*, 3(1), 35-40. doi: 10.1038/s41550-018-0658  
609 -y
- 610 Amann, F., Bonsignorio, F., Bulik, T., Bulten, H. J., Cuccuru, S., Dassargues, A.,  
611 ... Vasuth, M. (2020, March). Site-selection criteria for the Einstein Tele-  
612 scope. *arXiv e-prints*, arXiv:2003.03434.
- 613 Badaracco, F., & Harms, J. (2019, June). Optimization of seismometer arrays  
614 for the cancellation of Newtonian noise from seismic body waves. *Classical*  
615 *and Quantum Gravity*, 36(14), 145006. Retrieved from [https://doi.org/](https://doi.org/10.1088/1361-6382/ab28c1)  
616 [10.1088/1361-6382/ab28c1](https://doi.org/10.1088/1361-6382/ab28c1) doi: 10.1088/1361-6382/ab28c1
- 617 Badaracco, F., Harms, J., Bertolini, A., Bulik, T., Fiori, I., Idzkowski, B., ...  
618 Suchinski, M. (2020, May). Machine learning for gravitational-wave detec-  
619 tion: surrogate Wiener filtering for the prediction and optimized cancellation  
620 of Newtonian noise at Virgo. *arXiv e-prints*, arXiv:2005.09289.
- 621 Bard, P.-Y. (1982, December). Diffracted waves and displacement field over two-  
622 dimensional elevated topographies. *Geophysical Journal of the Royal Astro-*  
623 *nomical Society*, 71(3), 731-760. doi: 10.1111/j.1365-246X.1982.tb02795.x
- 624 Barsotti, L., Harms, J., & Schnabel, R. (2019, January). Squeezed vacuum states  
625 of light for gravitational wave detectors. *Reports on Progress in Physics*, 82(1),  
626 016905. doi: 10.1088/1361-6633/aab906
- 627 Basini, P., Liu, Q., & Tape, C. (2012, December). Ambient-noise Tomography of  
628 the Southern California Lithosphere. In *Agu fall meeting abstracts* (Vol. 2012,  
629 p. S41A-2415).
- 630 Basini, P., Nissen-Meyer, T., Boschi, L., Casarotti, E., Verbeke, J., Schenk, O., &  
631 Giardini, D. (2013, May). The influence of nonuniform ambient noise on  
632 crustal tomography in Europe. *Geochemistry, Geophysics, Geosystems*, 14(5),  
633 1471-1492. doi: 10.1002/ggge.20081
- 634 Beccaria, M., Bernardini, M., Braccini, S., Bradaschia, C., Bozzi, A., Casciano, C.,  
635 ... Zhang, Z. (1998). Relevance of Newtonian seismic noise for the VIRGO  
636 interferometer sensitivity. *Classical and Quantum Gravity*, 15(11), 3339.  
637 Retrieved from <http://stacks.iop.org/0264-9381/15/i=11/a=004>
- 638 Beker, M., Cella, G., DeSalvo, R., Doets, M., Grote, H., Harms, J., ... van Leeuwen,  
639 C. (2011). Improving the sensitivity of future GW observatories in the 1  
640 - 10Hz band: Newtonian and seismic noise. *General Relativity and Grav-*  
641 *itation*, 43(2), 623-656. Retrieved from [http://dx.doi.org/10.1007/](http://dx.doi.org/10.1007/s10714-010-1011-7)  
642 [s10714-010-1011-7](http://dx.doi.org/10.1007/s10714-010-1011-7) doi: 10.1007/s10714-010-1011-7
- 643 Beker, M. G., van den Brand, J. F. J., Hennes, E., & Rabeling, D. S. (2012).

- 644 Newtonian noise and ambient ground motion for gravitational wave detec-  
 645 tors. *Journal of Physics: Conference Series*, 363(1), 012004. Retrieved from  
 646 <http://stacks.iop.org/1742-6596/363/i=1/a=012004>
- 647 Beker, M. G., van den Brand, J. F. J., & Rabeling, D. S. (2015). Subterranean  
 648 ground motion studies for the Einstein Telescope. *Classical and Quantum*  
 649 *Gravity*, 32(2), 025002. Retrieved from [http://stacks.iop.org/0264-9381/](http://stacks.iop.org/0264-9381/32/i=2/a=025002)  
 650 [32/i=2/a=025002](http://stacks.iop.org/0264-9381/32/i=2/a=025002)
- 651 Blacker, T., Quadros, R. W., Owen, S. J., Staten, M. L., Hanks, B., Clark, B., ...  
 652 Ressler, P. (2019). *Trelis v16.5 [software]*.
- 653 Bonnefoy-Claudet, S., Cotton, F., & Bard, P.-Y. (2006). The nature of  
 654 noise wavefield and its applications for site effects studies: A literature  
 655 review. *Earth-Science Reviews*, 79(3-4), 205 - 227. Retrieved from  
 656 <http://www.sciencedirect.com/science/article/pii/S0012825206001012>  
 657 doi: <http://dx.doi.org/10.1016/j.earscirev.2006.07.004>
- 658 Cella, G. (2000). Off-Line Subtraction of Seismic Newtonian Noise. In  
 659 B. Casciaro, D. Fortunato, M. Francaviglia, & A. Masiello (Eds.), *Recent*  
 660 *developments in general relativity* (p. 495-503). Springer Milan. Re-  
 661 trieved from [http://dx.doi.org/10.1007/978-88-470-2113-6\\_44](http://dx.doi.org/10.1007/978-88-470-2113-6_44) doi:  
 662 [10.1007/978-88-470-2113-6\\_44](http://dx.doi.org/10.1007/978-88-470-2113-6_44)
- 663 Chan, M. L., Messenger, C., Heng, I. S., & Hendry, M. (2018, June). Binary neutron  
 664 star mergers and third generation detectors: Localization and early warning.  
 665 *Physical Review D*, 97, 123014. Retrieved from [https://link.aps.org/doi/](https://link.aps.org/doi/10.1103/PhysRevD.97.123014)  
 666 [10.1103/PhysRevD.97.123014](https://link.aps.org/doi/10.1103/PhysRevD.97.123014) doi: 10.1103/PhysRevD.97.123014
- 667 Coughlin, M., & Harms, J. (2012). Seismic topographic scattering in the context of  
 668 GW detector site selection. *Classical and Quantum Gravity*, 29, 075004. Re-  
 669 trieved from <http://stacks.iop.org/0264-9381/29/i=7/a=075004>
- 670 Coughlin, M., Harms, J., Bowden, D. C., Meyers, P., Tsai, V. C., Mandic, V., ...  
 671 Prestegard, T. (2019). Coherence-based approaches for estimating the compo-  
 672 sition of the seismic wavefield. *Journal of Geophysical Research: Solid Earth*,  
 673 124(3), 2941-2956. Retrieved from [https://agupubs.onlinelibrary.wiley](https://agupubs.onlinelibrary.wiley.com/doi/abs/10.1029/2018JB016608)  
 674 [.com/doi/abs/10.1029/2018JB016608](https://agupubs.onlinelibrary.wiley.com/doi/abs/10.1029/2018JB016608) doi: 10.1029/2018JB016608
- 675 Coughlin, M., Mukund, N., Harms, J., Driggers, J., Adhikari, R., & Mitra, S. (2016).  
 676 Towards a first design of a Newtonian-noise cancellation system for Advanced  
 677 LIGO. *Classical and Quantum Gravity*, 33(24), 244001. Retrieved from  
 678 <http://stacks.iop.org/0264-9381/33/i=24/a=244001>
- 679 Dahlen, F., & Tromp, J. (1998). *Theoretical global seismology*. Princeton university  
 680 press.
- 681 Driggers, J. C., Harms, J., & Adhikari, R. X. (2012, November). Subtrac-  
 682 tion of Newtonian noise using optimized sensor arrays. *Physical Review*  
 683 *D*, 86, 102001. Retrieved from [http://link.aps.org/doi/10.1103/](http://link.aps.org/doi/10.1103/PhysRevD.86.102001)  
 684 [PhysRevD.86.102001](http://link.aps.org/doi/10.1103/PhysRevD.86.102001) doi: 10.1103/PhysRevD.86.102001
- 685 ET Science Team. (2011). Einstein gravitational wave Telescope conceptual design  
 686 study. available from *European Gravitational Observatory, document number*  
 687 *ET-0106C-10*.
- 688 Fan, Y., & Snieder, R. (2009, November). Required source distribution for inter-  
 689 ferometry of waves and diffusive fields. *Geophysical Journal International*,  
 690 179(2), 1232-1244. doi: 10.1111/j.1365-246X.2009.04358.x
- 691 Fiorucci, D., Harms, J., Barsuglia, M., Fiori, I., & Paoletti, F. (2018, March).  
 692 Impact of infrasound atmospheric noise on gravity detectors used for astro-  
 693 physical and geophysical applications. *Physical Review D*, 97, 062003. Re-  
 694 trieved from <https://link.aps.org/doi/10.1103/PhysRevD.97.062003> doi:  
 695 [10.1103/PhysRevD.97.062003](https://link.aps.org/doi/10.1103/PhysRevD.97.062003)
- 696 Gilbert, F., & Knopoff, L. (1960). Seismic scattering from topographic irregularities.  
 697 *Journal of Geophysical Research*, 65(10), 3437-3444. Retrieved from [http://](http://dx.doi.org/10.1029/JZ065i010p03437)  
 698 [dx.doi.org/10.1029/JZ065i010p03437](http://dx.doi.org/10.1029/JZ065i010p03437) doi: 10.1029/JZ065i010p03437

- 699 Giunchi, C., Di Giovanni, M., Saccorotti, G., & Naticchioni, L. (2020, May).  
700 *Seismic noise characterization of the Sos Enattos Mine (Sardinia), a can-*  
701 *didate site for the next generation of terrestrial gravitational waves de-*  
702 *tectors.* (EGU General Assembly 2020, Online, EGU2020-9692) doi:  
703 <https://doi.org/10.5194/egusphere-egu2020-9692>
- 704 Grimm, S., & Harms, J. (2020, April). Multiband Gravitational Wave Parameter Es-  
705 timation: A Study of Future Detectors. *arXiv e-prints*, arXiv:2004.01434.
- 706 Gropp, W., Lusk, E., & Skjellum, A. (1994). *Using MPI, portable parallel program-*  
707 *ming with the Message-Passing Interface.* Cambridge, USA: MIT Press. doi:  
708 10.7551/mitpress/7056.001.0001
- 709 Hanasoge, S., Stehly, L., Nissen-Meyer, T., & Cupillard, P. (2012, December). Non-  
710 linear iterative inversions for the distribution of noise sources. In *Agu fall*  
711 *meeting abstracts* (Vol. 2012, p. S53C-2513).
- 712 Harms, J. (2019, October). Terrestrial gravity fluctuations. *Living Reviews in Rela-*  
713 *tivity*, 22(1), 6. Retrieved from [https://doi.org/10.1007/s41114-019-0022-](https://doi.org/10.1007/s41114-019-0022-2)  
714 [2](https://doi.org/10.1007/s41114-019-0022-2) doi: 10.1007/s41114-019-0022-2
- 715 Harms, J., Acernese, F., Barone, F., Bartos, I., Beker, M., van den Brand, J. F. J.,  
716 ... Wand, V. (2010). Characterization of the seismic environment at the San-  
717 ford Underground Laboratory, South Dakota. *Classical and Quantum Gravity*,  
718 27(22), 225011. Retrieved from [http://stacks.iop.org/0264-9381/27/](http://stacks.iop.org/0264-9381/27/i=22/a=225011)  
719 [i=22/a=225011](http://stacks.iop.org/0264-9381/27/i=22/a=225011)
- 720 Harms, J., Bonilla, E. L., Coughlin, M. W., Driggers, J., Dwyer, S. E., McManus,  
721 D. J., ... Venkateswara, K. (2020, May). Observation of a potential future  
722 sensitivity limitation from ground motion at LIGO Hanford. *Physical Re-*  
723 *view D*, 101, 102002. Retrieved from [https://link.aps.org/doi/10.1103/](https://link.aps.org/doi/10.1103/PhysRevD.101.102002)  
724 [PhysRevD.101.102002](https://link.aps.org/doi/10.1103/PhysRevD.101.102002) doi: 10.1103/PhysRevD.101.102002
- 725 Hild, S., Abernathy, M., Acernese, F., Amaro-Seoane, P., Andersson, N., Arun, K.,  
726 ... Yamamoto, K. (2011). Sensitivity studies for third-generation gravitational  
727 wave observatories. *Classical and Quantum Gravity*, 28(9), 094013. Retrieved  
728 from <http://stacks.iop.org/0264-9381/28/i=9/a=094013>
- 729 Hild, S., Chelkowski, S., Freise, A., Franc, J., Morgado, N., Flaminio, R., & DeSalvo,  
730 R. (2009, December). A xylophone configuration for a third-generation gravita-  
731 tional wave detector. *Classical and Quantum Gravity*, 27(1), 015003. Retrieved  
732 from <https://doi.org/10.1088/0264-9381/27/1/015003> doi:  
733 10.1088/0264-9381/27/1/015003
- 734 Hudson, J., & Knopoff, L. (1967, January). Statistical properties of rayleigh waves  
735 due to scattering by topography. *Bulletin of the Seismological Society of Amer-*  
736 *ica*, 57, 83-90.
- 737 Hudson, J. A. (1967). Scattered Surface Waves from a Surface Obstacle.  
738 *Geophysical Journal International*, 13(4), 441-458. Retrieved from  
739 <http://gji.oxfordjournals.org/content/13/4/441.abstract> doi:  
740 10.1111/j.1365-246X.1967.tb03143.x
- 741 Hudson, J. A., Humphryes, R. F., Mason, I. M., & Kembhavi, V. K. (1973, Decem-  
742 ber). The scattering of longitudinal elastic waves at a rough free surface. *Jour-*  
743 *nal of Physics D Applied Physics*, 6(18), 2174-2186. doi: 10.1088/0022-3727/6/  
744 18/303
- 745 Hughes, S. A., & Thorne, K. S. (1998, November). Seismic gravity-gradient noise in  
746 interferometric gravitational-wave detectors. *Physical Review D*, 58, 122002.  
747 Retrieved from <http://link.aps.org/doi/10.1103/PhysRevD.58.122002>  
748 doi: 10.1103/PhysRevD.58.122002
- 749 Komatitsch, D. (2004, February). Simulations of Ground Motion in the Los Ange-  
750 les Basin Based upon the Spectral-Element Method. *The Bulletin of the Seis-*  
751 *mological Society of America*, 94(1), 187-206. doi: 10.1785/0120030077
- 752 Komatitsch, D., Labarta, J., & Michéa, D. (2008). A simulation of seismic wave  
753 propagation at high resolution in the inner core of the Earth on 2166 proces-

- 754 sors of MareNostrum. *Lecture Notes in Computer Science*, 5336, 364-377. doi:  
755 10.1007/978-3-540-92859-1\\_33
- 756 Komatitsch, D., & Martin, R. (2007, January). An unsplit convolutional perfectly  
757 matched layer improved at grazing incidence for the seismic wave equation.  
758 *Geophysics*, 72(5), SM155. doi: 10.1190/1.2757586
- 759 Komatitsch, D., & Tromp, J. (1999). Introduction to the spectral element method  
760 for three-dimensional seismic wave propagation. *Geophysical Journal Interna-*  
761 *tional*, 139(3), 806–822. Retrieved from [http://dx.doi.org/10.1046/j.1365-](http://dx.doi.org/10.1046/j.1365-246x.1999.00967.x)  
762 [246x.1999.00967.x](http://dx.doi.org/10.1046/j.1365-246x.1999.00967.x) doi: 10.1046/j.1365-246x.1999.00967.x
- 763 Komatitsch, D., & Tromp, J. (2002a). Spectral-element simulations of global seis-  
764 mic wave propagation I. Validation. *Geophysical Journal International*, 149(2),  
765 390-412. Retrieved from [http://gji.oxfordjournals.org/content/149/2/](http://gji.oxfordjournals.org/content/149/2/390.abstract)  
766 [390.abstract](http://gji.oxfordjournals.org/content/149/2/390.abstract) doi: 10.1046/j.1365-246X.2002.01653.x
- 767 Komatitsch, D., & Tromp, J. (2002b). Spectral-element simulations of global  
768 seismic wave propagation—ii. three-dimensional models, oceans, rotation  
769 and self-gravitation. *Geophysical Journal International*, 150(1), 303-318.  
770 Retrieved from [https://onlinelibrary.wiley.com/doi/abs/10.1046/](https://onlinelibrary.wiley.com/doi/abs/10.1046/j.1365-246X.2002.01716.x)  
771 [j.1365-246X.2002.01716.x](https://onlinelibrary.wiley.com/doi/abs/10.1046/j.1365-246X.2002.01716.x) doi: 10.1046/j.1365-246X.2002.01716.x
- 772 Komatitsch, D., Tsuboi, S., Ji, C., & Tromp, J. (2003, November). A 14.6 billion  
773 degrees of freedom, 5 teraflops, 2.5 terabyte earthquake simulation on the  
774 Earth Simulator. In *Proceedings of the sc'03 acm/ieee conference on supercom-*  
775 *puting* (p. 4-11). Phoenix, Arizona, USA: ACM. (Gordon Bell Prize winner  
776 article) doi: 10.1145/1048935.1050155
- 777 Komatitsch, D., & Vilotte, J.-P. (1998). The spectral element method: An efficient  
778 tool to simulate the seismic response of 2D and 3D geological structures. *Bul-*  
779 *letin of the Seismological Society of America*, 88(2), 368-392. Retrieved from  
780 <http://www.bssaonline.org/content/88/2/368.abstract>
- 781 Komatitsch, D., Vilotte, J.-P., Afanasiev, M., Ampuero, J.-P., Bachmann, E., Bai,  
782 K., ... Zhu, H. (2018). *Specfem 3d cartesian v3.0 [software]*.
- 783 Komatitsch, D., Vilotte, J.-P., Vai, R., Castillo-Covarrubias, J. M., & Sánchez-  
784 Sesma, F. J. (1999, July). The spectral element method for elastic wave  
785 equations—application to 2-D and 3-D seismic problems. *International*  
786 *Journal for Numerical Methods in Engineering*, 45(9), 1139-1164. doi:  
787 10.1002/(SICI)1097-0207(19990730)45:9<1139::AID-NME617>3.0.CO;2-T
- 788 Liu, Q., & Tromp, J. (2006, December). Finite-Frequency Kernels Based on Adjoint  
789 Methods. *The Bulletin of the Seismological Society of America*, 96(6), 2383-  
790 2397. doi: 10.1785/0120060041
- 791 Liu, Q., & Tromp, J. (2008, July). Finite-frequency sensitivity kernels for global seis-  
792 mic wave propagation based upon adjoint methods. *Geophysical Journal Inter-*  
793 *national*, 174(1), 265-286. doi: 10.1111/j.1365-246X.2008.03798.x
- 794 Maday, Y., & Patera, A. T. (1989, January). Spectral element methods for the in-  
795 compressible Navier-Stokes equations. In *In: State-of-the-art surveys on com-*  
796 *putational mechanics (a90-47176 21-64). new york* (p. 71-143).
- 797 Maggiore, M., Broeck, C. V. D., Bartolo, N., Belgacem, E., Bertacca, D., Bizouard,  
798 M. A., ... Sakellariadou, M. (2020, March). Science case for the einstein tele-  
799 scope. *Journal of Cosmology and Astroparticle Physics*, 2020(03), 050–050.  
800 Retrieved from <https://doi.org/10.1088/1475-7516/2020/03/050>  
801 doi: 10.1088/1475-7516/2020/03/050
- 802 Mandic, V., Tsai, V. C., Pavlis, G. L., Prestegard, T., Bowden, D. C., Meyers, P.,  
803 & Caton, R. (2018). A 3D Broadband Seismometer Array Experiment at the  
804 Homestake Mine. *Seismological Research Letters*, 89(6), 2420. Retrieved from  
805 <http://dx.doi.org/10.1785/0220170228> doi: 10.1785/0220170228
- 806 Maradudin, A., & Mills, D. (1976, September). Attenuation of rayleigh surface  
807 waves by surface roughness. *Annals of Physics*, 100, 262-309. doi: 10.1016/  
808 0003-4916(76)90063-4

- 809 Martin, R., & Komatitsch, D. (2009, October). An unsplit convolutional perfectly  
 810 matched layer technique improved at grazing incidence for the viscoelastic  
 811 wave equation. *Geophysical Journal International*, 179(1), 333-344. doi:  
 812 10.1111/j.1365-246X.2009.04278.x
- 813 Martin, R., Komatitsch, D., Gedney, S., & Bruthiaux, E. (2010, January). A  
 814 high-order time and space formulation of the unsplit perfectly matched layer  
 815 for the seismic wave equation using auxiliary differential equations (ade-  
 816 pml). *Computer Modelling in Engineering and Sciences - CMES*, 56. doi:  
 817 10.3970/cmcs.2010.056.017
- 818 Matchard, F., Lantz, B., Mason, K., Mittleman, R., Abbott, B., Abbott, S., ...  
 819 Warner, J. (2014). Advanced LIGO two-stage twelve-axis vibration isolation  
 820 and positioning platform. Part 1: Design and production overview. *Preci-  
 821 sion Engineering*(0), -. Retrieved from [http://www.sciencedirect.com/  
 822 science/article/pii/S0141635914001561](http://www.sciencedirect.com/science/article/pii/S0141635914001561) doi: [http://dx.doi.org/10.1016/  
 823 j.precisioneng.2014.09.010](http://dx.doi.org/10.1016/j.precisioneng.2014.09.010)
- 824 Mooney, H. M. (1976). The seismic wave system from a surface impact. *Geophysics*,  
 825 41(2), 243-265. Retrieved from [http://geophysics.geoscienceworld.org/  
 826 content/41/2/243.abstract](http://geophysics.geoscienceworld.org/content/41/2/243.abstract) doi: 10.1190/1.1440614
- 827 Ogilvy, J. A. (1987). Wave scattering from rough surfaces. *Reports on Progress in  
 828 Physics*, 50(12), 1553. Retrieved from [http://stacks.iop.org/0034-4885/  
 829 50/i12/a12](http://stacks.iop.org/0034-4885/50/i12/a12) doi: 10.1088/0034-4885/50/12/001
- 830 Olsen, K. B., Madariaga, R., & Archuleta, R. J. (1997, October). Three-Dimensional  
 831 Dynamic Simulation of the 1992 Landers Earthquake. *Science*, 278, 834-838.  
 832 doi: 10.1126/science.278.5339.834
- 833 Orfanidis, S. J. (2007). *Optimum signal processing: an introduction*. Macmillan pub-  
 834 lishing company.
- 835 Otto, O. W. (1977, December). Scattering of Rayleigh waves from topographic irreg-  
 836 ularities at oblique incidence. *Journal of Applied Physics*, 48(12), 5105-5110.  
 837 doi: 10.1063/1.323587
- 838 Pacheco, P. S. (1997). *Parallel programming with MPI*. San Francisco, USA: Morgan  
 839 Kaufmann Press.
- 840 Patera, A. T. (1984, June). A Spectral Element Method for Fluid Dynamics: Lam-  
 841 inar Flow in a Channel Expansion. *Journal of Computational Physics*, 54(3),  
 842 468-488. doi: 10.1016/0021-9991(84)90128-1
- 843 Peter, D., Komatitsch, D., Luo, Y., Martin, R., Le Goff, N., Casarotti, E., ...  
 844 Tromp, J. (2011). Forward and adjoint simulations of seismic wave propa-  
 845 gation on fully unstructured hexahedral meshes. *Geophysical Journal Interna-  
 846 tional*, 186(2), 721-739. doi: 10.1111/j.1365-246X.2011.05044.x
- 847 Peter, D., Tape, C., Boschi, L., & Woodhouse, J. H. (2007, December). Surface wave  
 848 tomography: global membrane waves and adjoint methods. *Geophysical Jour-  
 849 nal International*, 171(3), 1098-1117. doi: 10.1111/j.1365-246X.2007.03554.x
- 850 Priolo, E., Carcione, J. M., & Seriani, G. (1994, February). Numerical simulation of  
 851 interface waves by high-order spectral modeling techniques. *Acoustical Society  
 852 of America Journal*, 95(2), 681-693. doi: 10.1121/1.408428
- 853 Punturo, M., Abernathy, M., Acernese, F., Allen, B., Andersson, N., Arun, K., ...  
 854 Yamamoto, K. (2010). The Einstein Telescope: a third-generation gravita-  
 855 tional wave observatory. *Classical and Quantum Gravity*, 27(19), 194002.  
 856 Retrieved from <http://stacks.iop.org/0264-9381/27/i=19/a=194002>
- 857 Sanchez-Sesma, F., & Campillo, M. (1991, January). Diffraction of p, sv and  
 858 rayleigh waves by topographic features: a boundary integral formulation. *Bul-  
 859 letin - Seismological Society of America*, 81(6), 2234-2253.
- 860 Sathyaprakash, B., Abernathy, M., Acernese, F., Ajith, P., Allen, B., Amaro-  
 861 Seoane, P., ... Yamamoto, K. (2012). Scientific objectives of einstein tele-  
 862 scope. *Classical and Quantum Gravity*, 29(12), 124013. Retrieved from  
 863 <http://stacks.iop.org/0264-9381/29/i=12/a=124013>

- 864 Souradeep, T. (2016). LIGO-India. *Resonance*, *21*, 225 – 231. Retrieved  
865 from <https://doi.org/10.1007/s12045-016-0316-6> doi: 10.1007/  
866 s12045-016-0316-6
- 867 Tromp, J., Komatitsch, D., & Liu, Q. (2008). Spectral-element and adjoint methods  
868 in seismology. *Communications in Computational Physics*, *3*(1), 1-32.
- 869 Tromp, J., Luo, Y., Hanasoge, S., & Peter, D. (2010, November). Noise cross-  
870 correlation sensitivity kernels. *Geophysical Journal International*, *183*(2),  
871 791-819. doi: 10.1111/j.1365-246X.2010.04721.x
- 872 Tromp, J., Tape, C., & Liu, Q. (2005, January). Seismic tomography, adjoint meth-  
873 ods, time reversal and banana-doughnut kernels. *Geophysical Journal Interna-*  
874 *tional*, *160*(1), 195-216. doi: 10.1111/j.1365-246X.2004.02453.x
- 875 Tsai, V. C., & Moschetti, M. P. (2010, July). An explicit relationship be-  
876 tween time-domain noise correlation and spatial autocorrelation (SPAC)  
877 results. *Geophysical Journal International*, *182*(1), 454-460. doi: 10.1111/  
878 j.1365-246X.2010.04633.x
- 879 Tsuboi, S., Komatitsch, D., Ji, C., & Tromp, J. (2003, October). Broadband model-  
880 ing of the 2002 Denali fault earthquake on the Earth Simulator. *Physics of the*  
881 *Earth and Planetary Interiors*, *139*(3-4), 305-313. doi: 10.1016/j.pepi.2003.09  
882 .012
- 883 Virieux, J. (1986, April). P-SV wave propagation in heterogeneous media: Velocity-  
884 stress finite-difference method. *Geophysics*, *51*(4), 889-901. doi: 10.1190/  
885 .1442147
- 886 Wapenaar, K., Slob, E., & Snieder, R. (2006, December). Unified Green's Function  
887 Retrieval by Cross Correlation. *Physical Review Letters*, *97*(23), 234301. doi:  
888 10.1103/PhysRevLett.97.234301
- 889 Woodard, M. F. (1997, August). Implications of Localized, Acoustic Absorption  
890 for Heliotomographic Analysis of Sunspots. *The Astrophysical Journal*, *485*(2),  
891 890-894. doi: 10.1086/304468
- 892 Woods, R. D. (1968). Screening of Surface Waves in Soils. *Journal of the Soil Me-*  
893 *chanics and Foundations Division: proceedings of the American Society of Civil*  
894 *Engineers*, *94*(4), 951-979.
- 895 Xie, Z., Komatitsch, D., Martin, R., & Matzen, R. (2014, September). Improved for-  
896 ward wave propagation and adjoint-based sensitivity kernel calculations using  
897 a numerically stable finite-element PML. *Geophysical Journal International*,  
898 *198*(3), 1714-1747. doi: 10.1093/gji/ggu219